

Optical Time-Frequency Packing: Principles, Design, Implementation, and Experimental Demonstration

Marco Secondini *Member, IEEE*, Tommaso Foggi, Francesco Fresi, Gianluca Meloni, Fabio Cavaliere *Member, IEEE*, Giulio Colavolpe *Senior Member, IEEE*, Enrico Forestieri *Member, IEEE*, Luca Potì *Member, IEEE*, Roberto Sabella *Senior Member, IEEE*, and Giancarlo Prati *Fellow, IEEE*

Abstract—Time-frequency packing (TFP) transmission provides the highest achievable spectral efficiency with a constrained symbol alphabet and detector complexity. In this work, the application of the TFP technique to fiber-optic systems is investigated and experimentally demonstrated. The main theoretical aspects, design guidelines, and implementation issues are discussed, focusing on those aspects which are peculiar to TFP systems. In particular, adaptive compensation of propagation impairments, matched filtering, and maximum a posteriori probability detection are obtained by a combination of a butterfly equalizer and four 8-state parallel Bahl-Cocke-Jelinek-Raviv (BCJR) detectors. A novel algorithm that ensures adaptive equalization, channel estimation, and a proper distribution of tasks between the equalizer and BCJR detectors is proposed. A set of irregular low-density parity-check codes with different rates is designed to operate at low error rates and approach the spectral efficiency limit achievable by TFP at different signal-to-noise ratios. An experimental demonstration of the designed system is finally provided with five dual-polarization QPSK-modulated optical carriers, densely packed in a 100 GHz bandwidth, employing a recirculating loop to test the performance of the system at different transmission distances.

Index Terms—Time-frequency packing, faster-than-Nyquist signaling, information theory, optical fiber communication, coherent optical systems.

I. INTRODUCTION

Next generation optical systems will use coherent detection and advanced signal processing for enabling the transmission of extremely high bit rates. Currently deployed 100 Gb/s single-carrier systems typically operate on a 50 GHz grid spacing, employing quadrature phase-shift keying (QPSK) modulation with polarization multiplexing to meet the required

2 bit/s/Hz spectral efficiency (SE), with a potential reach of thousands of kilometers. This, considering the actual power and bandwidth limitations of typical fiber-optic links, still leaves a significant margin for improvement with respect to channel capacity. On the other hand, accommodating the ever increasing traffic demand will require, in the next years, to operate as close as possible to the Shannon limit, achieving a much higher SE and possibly adapting it to the available signal-to-noise ratio (SNR). While the use of coherent detection, digital signal processing (DSP), and soft-decision forward error correction is not in question in long-haul systems, a few different options are being considered for the optical transport format. Besides a high SE, the selected format should also offer best performance in terms of energy efficiency, cost, and reliability, the complexity of the required DSP being one of the driving factors for all those issues. From a system point of view, the whole problem can be summarized as finding the best combination of modulation and coding that maximizes SE for a given SNR and constrained complexity. In optical communications, orthogonal signaling is typically adopted to ensure the absence of inter-symbol interference (ISI) and inter-carrier interference (ICI). For instance, both Nyquist wavelength-division multiplexing (WDM) [1] and orthogonal frequency-division multiplexing (OFDM) [2] solutions, whose performance and complexity are basically equivalent on the fiber-optic channel [3], employ orthogonal signaling. In both cases, the orthogonality condition sets a lower limit to time- and frequency-spacing (the Nyquist criterion), such that the achievable SE is limited by the number of levels of the underlying modulation format. In fact, higher SE requires higher-order modulation (e.g., 16-ary quadrature amplitude modulation (QAM)), with higher transmitter and receiver complexity.

Recently, a different approach has been proposed which, giving up the orthogonality condition, allows to overcome the Nyquist limit and achieve a higher SE with low-order modulations [4]–[8]. This time- and frequency-packing (TFP) approach is an extension of well known faster-than-Nyquist (FTN) signaling [9]. In Mazo FTN signaling, pulses are packed closer than the Nyquist limit without asymptotic performance degradation, provided that the minimum Euclidean distance of the system is not reduced and the optimum detector is employed (Mazo limit) [9]. Analogously, a closer packing can be achieved also in frequency domain without asymptotic per-

This work was supported in part by the Italian Ministry for Education University and Research (MIUR) under the FIRB project COTONE.

M. Secondini, F. Fresi, E. Forestieri, and G. Prati are with TeCIP Institute, Scuola Superiore Sant’Anna, 56124 Pisa, Italy, and with National Laboratory of Photonic Networks, CNIT, 56124 Pisa, Italy (email: marco.secondini@sss.up.it; francesco.fresi@sss.up.it; forestieri@sss.up.it; giancarlo.prati@cnit.it).

T. Foggi is with CNIT, 43124 Parma, Italy (email: tommaso.foggi@cnit.it).

G. Meloni and L. Potì are with National Laboratory of Photonic Networks, CNIT, 56124 Pisa, Italy (email: gianluca.meloni@cnit.it; luca.poti@cnit.it).

F. Cavaliere and R. Sabella are with Ericsson (email: fabio.cavaliere@ericsson.com; roberto.sabella@ericsson.com).

G. Colavolpe is with the Dipartimento di Ingegneria dell’Informazione, University of Parma, 43124 Parma, Italy (email: giulio@unipr.it).

Copyright (c) 2015 IEEE. Personal use of this material is permitted. However, permission to use this material for any other purposes must be obtained from the IEEE by sending a request to pubs-permissions@ieee.org.

formance degradation (two dimensional Mazo limit) [10]–[13]. In other words, by increasing signaling rate for a fixed pulse bandwidth (or, equivalently, by reducing pulse bandwidth for a fixed signaling rate), some bandwidth resources are saved at the expense of introducing ISI. A similar approach has been experimentally demonstrated also in [14]. FTN¹, however, does not provide the best performance in terms of SE, and has a limit in the complexity of the required detector (which can be very high). On the other hand, TFP overcomes this limit and seeks the best solution by dividing the problem in three parts: i) set the desired input constellation (e.g., QPSK) and detector complexity; ii) find the optimum time- and frequency-spacing which provide the maximum achievable SE for the given input constellation and detector complexity; iii) select a proper code to approach as close as desired the achievable SE (information theory guarantees that such a code exists).

In this work, after introducing the theoretical aspects of the TFP approach, we discuss the design procedure and implementation of a TFP fiber-optic system and experimentally investigate its performance. Section II introduces the TFP approach and the basic concept of achievable SE for a mismatched decoder, whose maximization is the key aspect of TFP. In Section III we explain how to design a TFP system and find the optimum modulation parameters (time and frequency spacing) that maximize the achievable SE for a given transmitter and receiver complexity. Moreover, we present a set of irregular low-density parity-check (LDPC) codes to practically approach the achievable SE. The practical implementation of a TFP fiber-optic system is discussed in Section IV, focusing on the DSP part, which is the only one to require some modifications with respect to a standard WDM system employing coherent detection. The experimental demonstration of the designed TFP system is addressed in Section V: five closely-packed 40 Gbd dual-polarization (DP) quaternary phase-shift keying (QPSK) channels are transmitted through a recirculating loop, keeping the net SE beyond the theoretical limit of Nyquist-WDM (4 bit/s/Hz) up to 6000 km; higher SEs are achieved at shorter distances by adapting the TFP configuration and code rate to the available OSNR, achieving a net SE of more than 7 bit/s/Hz (for DP-QPSK transmission) at a distance of 400 km. A discussion of the results is provided in Section VI and conclusions are finally drawn in Section VII.

II. TIME-FREQUENCY PACKING

In order to summarize the general ideas behind TFP, we refer here to an ideal dual-polarization AWGN channel. Rather than as a specific modulation format, TFP should be regarded as a design procedure for the optimization of a class of modulation formats—namely, multicarrier linear modulations, to which both Nyquist WDM and OFDM belong. Many communication systems employ this kind of modulation to encode information onto waveforms which can be practically generated and reliably transmitted through a given communication channel. The low-pass equivalent model of a generic

¹Here and in the rest of the paper, FTN refers to Mazo FTN, as originally proposed in [9].

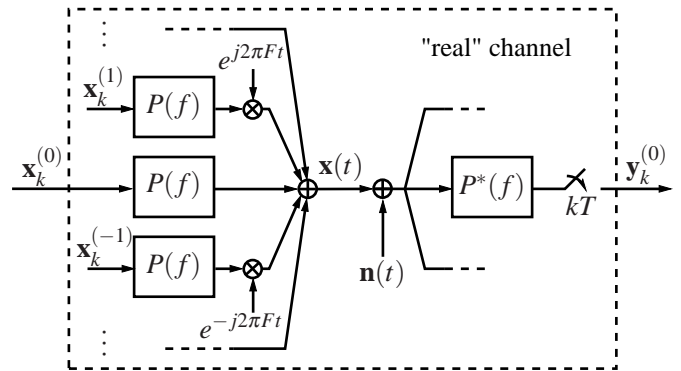


Figure 1. Low-pass equivalent model employed to design the TFP system

linearly-modulated multicarrier system is schematically depicted in Fig. 1. All the equally-spaced carriers are linearly modulated with the same modulation format and shaping pulse $p(t) = \mathcal{F}^{-1}\{P(f)\}$. The complex envelope of the transmitted signal is

$$\mathbf{x}(t) = \sum_{\ell=-M}^M \sum_{k=1}^K \mathbf{x}_k^{(\ell)} p(t - kT) e^{j2\pi\ell Ft} \quad (1)$$

where $\mathbf{x}_k^{(\ell)}$ is the transmitted symbol (a two-component vector, one per each polarization) on the ℓ -th carrier at time kT , T is the symbol time (or time spacing between adjacent symbols), F the frequency spacing between adjacent carriers, and, for simplicity, a perfect time and phase synchronization among the carriers is assumed². Signal (1) is corrupted by additive white Gaussian noise (AWGN) $\mathbf{n}(t)$ and demodulated by a bank of matched filters and symbol-time samplers. Assuming a system with $2M + 1$ carriers (a number sufficiently large to neglect border effects) and denoting by $\mathbf{x} = \{\mathbf{x}_k^{(\ell)}\}$ the set of transmitted symbols and by $\mathbf{y} = \{\mathbf{y}_k^{(\ell)}\}$ the set of channel outputs, the SE of the system (bit/s/Hz) is³

$$\eta = \frac{I(\mathbf{X}; \mathbf{Y})}{FT} \quad (2)$$

where $I(\mathbf{X}; \mathbf{Y})$ is the average mutual information rate (bit/symbol) between input and output [16], and $1/FT$ is the inverse of the time-frequency spacing product, which equals the number of symbols transmitted per second per Hertz. Typically, these modulation formats are designed to avoid both ISI and ICI by imposing proper orthogonality constraints on the employed waveforms (e.g., Nyquist-WDM or OFDM). This, in turn, poses a constraint on the pulse shape and sets a limit

²When employing single-user detectors, which is the case considered in this work, the actual phase and time shift between carriers is typically irrelevant and has a negligible impact on the achievable information rate, both in terms of linear cross-talk among carriers (which, as shown later, are only slightly overlapped), and of inter-channel nonlinearity [15]. In fact, the experimental demonstration of Section V does not employ any phase locking or time synchronization among carriers.

³Here, η denotes the maximum rate per unit bandwidth at which information can be reliably transmitted through the channel with i.i.d. input symbols, where maximization is performed over all possible encoding of information bits on transmitted symbols. In the following, we will also consider other two slightly different definitions of SE, where specific constraints on the detector or coding strategy are imposed. Moreover, upper-case letters denote random variables, while lower-case letters denote their realizations.

to the minimum time and frequency spacing between pulses (Nyquist limit). When this orthogonal signaling approach is employed, $I(\mathbf{X}; \mathbf{Y}) = I(\mathbf{X}_k^{(\ell)}; \mathbf{Y}_k^{(\ell)})$, $\forall k, \ell$ is achievable by a symbol-by-symbol detector⁴ and depends only on the modulation format and signal-to-noise ratio. On the other hand, the minimum value of the time-frequency spacing product at denominator of (2) is set by the Nyquist limit and is $FT = 1$ —achievable, for instance, by using pulses with a rectangular spectrum $P(f) = \sqrt{1/B} \text{rect}(f/B)$ of low-pass bandwidth $B/2$ and setting $F = B$ and $T = 1/B$, as in Nyquist-WDM [1]. Thus, the only way to increase η is through the numerator of (2), by increasing the cardinality of the modulation alphabet. The main drawback of this approach is that a high SE is obtained at the expense of strict requirements on spectral shaping and higher-order symbol alphabets. For orthogonal DP-QPSK modulation, the upper limit is $\eta = 4$ bit/s/Hz.

On the contrary, if we give up the orthogonality condition, we have no constraints on the choice of $p(t)$, F , and T . Thus, we can select a shaping pulse $p(t)$ that is compatible with the available hardware components, and try to increase (2) by reducing the denominator FT below the Nyquist limit, without changing the symbol alphabet. This way, however, we also introduce ICI and ISI and, therefore, reduce the numerator $I(\mathbf{X}; \mathbf{Y})$. Thus, we can transmit more symbols per unit time and frequency, but less information bits per symbol. Moreover, the presence of ICI and ISI makes $I(\mathbf{X}; \mathbf{Y})$ unachievable by a symbol-by-symbol detector. Thus, the problem is that of selecting F and T such that the decrease of the numerator of (2) is more than balanced by the decrease of the denominator, for any allotted complexity of the required detector. In Mazo FTN signaling, T is selected as the minimum value for which the minimum Euclidean distance of the system is not reduced (Mazo limit) [9]. Thus, pulses are packed closer than the Nyquist limit without performance degradation, provided that the optimum sequence detector is employed. Analogously, a closer packing can be achieved also in frequency domain without performance degradation (two-dimensional Mazo limit) [10]–[13]. This approach, however, does not provide the best performance in terms of (2) and poses no constraints on the complexity of the required detector.

The TFP approach, instead, allows to introduce, for a given constellation, an arbitrary constraint on the detector complexity (meant as specified later) and optimize the time and frequency spacings in order to maximize the spectral efficiency achievable by that constrained-complexity detector when using that constellation. To this aim—limiting the analysis to single-user detectors (which is a practical choice to limit the detector complexity) and focusing, without loss of generality, on the central carrier ($\ell = 0$), such that the others are considered only as a source of ICI and are, therefore, a part of the “real” channel depicted in Fig. 1—a slightly different (and more practical, as shown later) definition of SE is adopted by replacing the mutual information rate $I(\mathbf{X}; \mathbf{Y})$ in (2) with the achievable information rate (AIR) for a mismatched

decoder [17]

$$\hat{I}(\mathbf{X}^{(0)}; \mathbf{Y}^{(0)}) \triangleq \lim_{K \rightarrow \infty} \frac{1}{K} E \left\{ \log \frac{q(\mathbf{y}^{(0)} | \mathbf{x}^{(0)})}{q(\mathbf{y}^{(0)})} \right\} \leq I(\mathbf{X}; \mathbf{Y}) \quad (3)$$

where vectors $\mathbf{x}^{(0)}$ and $\mathbf{y}^{(0)}$ collect, respectively, the K transmitted symbols and K received samples on the “real” channel depicted in Fig. 1, expectation $E\{\cdot\}$ is taken with respect to the real channel, while $q(\mathbf{y}^{(0)} | \mathbf{x}^{(0)})$ and $q(\mathbf{y}^{(0)})$ are, respectively, the conditional and marginal output distribution obtained by connecting inputs to an arbitrary auxiliary channel—equality holding if $q(\mathbf{y}^{(0)} | \mathbf{x}^{(0)})$ and $q(\mathbf{y}^{(0)})$ equal the distributions of the real channel. The importance of the quantity defined in (3) is in its properties, which hold for any real and auxiliary channel: it is a lower bound to the mutual information rate $I(\mathbf{X}; \mathbf{Y})$ on the real channel; it is achievable by the maximum *a posteriori* probability (MAP) detector designed for the selected auxiliary channel; and it can be simply evaluated through simulations [18]. The auxiliary channel, though arbitrary, is conveniently chosen as the one providing the best trade-off between performance and complexity: the closer the auxiliary channel to the real channel, the higher is the AIR $\hat{I}(\mathbf{X}^{(0)}; \mathbf{Y}^{(0)})$ (and closer to $I(\mathbf{X}; \mathbf{Y})$); the simpler the auxiliary channel, the simpler is the MAP detector required to achieve $\hat{I}(\mathbf{X}^{(0)}; \mathbf{Y}^{(0)})$. Finally, time and frequency spacing are optimized by maximizing the achievable SE with the selected detector

$$\hat{\eta}_{\max} = \max_{F, T > 0} \frac{\hat{I}(\mathbf{X}^{(0)}; \mathbf{Y}^{(0)})}{FT} \leq \eta. \quad (4)$$

Optimization (4) is the very essence of TFP, which distinguishes it from FTN or other non-orthogonal signaling techniques. The result obtained through (4) depends on the shaping pulse $p(t)$ considered in (1), though any scaling of the pulse in time domain can be easily accounted for by properly rescaling T and F . The maximum achievable SE depends also on the given SNR (it increases as the SNR increases). However, the optimum F and T depend only slightly on it, such that a single optimization can be adopted for a wide range of SNRs (i.e., of link distances).

The last step of the TFP method is common to almost any digital communication system and consists in finding a coding strategy that, by properly encoding information bits on transmitted symbols $\{\mathbf{x}_k^{(0)}\}$, operates arbitrarily closely to (4)—information theory guarantees that such a code does exist. Though similar coding strategies can be adopted in TFP and orthogonal signaling, this step has some peculiarities related to the presence of ISI and ICI which will be discussed in the next section.

III. SYSTEM DESIGN

In this section, we show how to design a multicarrier fiber-optic system by employing the TFP approach described in the previous section. We refer, again, to the ideal low-pass equivalent scheme reported in Fig. 1, which, under some assumptions, is a reasonable representation of the fiber-optic

⁴Note that with symbol-by-symbol detector we mean a simple threshold detector not working on a trellis. So, according to our definition, a BCJR detector is not a symbol-by-symbol detector.

channel,⁵ and consider a DP-QPSK modulation alphabet. A sequence of i.i.d. symbols $\{\mathbf{x}_k\}$, drawn from a DP-QPSK alphabet, modulates the selected carrier ($\ell = 0$, in the scheme) at rate $1/T$ with a real shaping pulse $p(t)$. All the modulated carriers are then combined and transmitted through an AWGN channel with noise $\mathbf{n}(t)$. At the receiver, the selected carrier is demodulated by a matched filter and a symbol-time sampler. Received samples $\{\mathbf{y}_k\}$ are finally sent to a MAP symbol detector that operates on the output of the matched filter [19], [20] and is implemented through the algorithm by Bahl, Cocke, Jelinek, and Raviv (BCJR) [21]. The MAP symbol detector is matched to an auxiliary channel, whose selection determines the distributions $q(\mathbf{y}^{(0)}|\mathbf{x}^{(0)})$ and $q(\mathbf{y}^{(0)})$ to be used in (3). In particular, as an auxiliary channel we take an approximation of the real channel, obtained from the latter by neglecting ICI, truncating ISI to the first $L_T \leq L$ pre- and post-cursor symbols (after the matched filter)—where $2L + 1$ is the actual memory of the channel and L_T is a design parameter strictly related to detector complexity—and increasing the variance of the noise samples at the output of the matched filter from the actual value σ_n^2 to a numerically optimized value $\sigma_{n'}^2 > \sigma_n^2$ to account for the neglected ICI and ISI. This choice provides a reasonable trade-off between performance (how tight is the bound in (3)) and complexity (of the matched BCJR detector). Moreover, when a Gray-mapping is used, the DP-QPSK modulation can be seen as the combination of four orthogonal BPSK modulations, one per each quadrature component of each state of polarization of the signal. Thus, four independent and identical BCJR detectors with 2^{L_T} states are used to separately detect the four BPSK components that are transmitted over four independent and identical channels with memory $2L_T + 1$.

Although also the pulse shape $p(t)$ can be optimized to maximize the SE [22], in this work we consider only the pulse shape obtained by employing a ninth-order type I Chebyshev filter with 3 dB bandwidth B , which approximately models the electrical low-pass filters available in our laboratory for the experimental implementation described in Section V. For the given shape, (3) is evaluated through numerical simulations as explained in [18] on a grid of values of the normalized time and frequency spacing TB and F/B , seeking the maximum SE (4) and the corresponding optimum spacings. To account for unsynchronized channels and unlocked lasers, each modulated carrier is also subject to a random phase and time shift and polarization rotation. The optimization is performed considering a truncated channel memory $2L_T + 1 = 7$ (requiring 8-state MAP symbol detectors) and two different values of the SNR per bit (defined as the ratio E_b/N_0 between the mean energy per bit and the noise power spectral density and related to the OSNR through $\text{OSNR} = R_b E_b / (2N_0 B_{\text{ref}})$, where R_b is the total net bit rate and $B_{\text{ref}} \simeq 12.5$ GHz the

conventional reference bandwidth) of 7.5 and 22.5 dB. The corresponding contour plots of the achievable SE are reported in Fig. 2(a) and (b). It can be noticed that the optimum configuration is obtained with a significant overlap of pulses in time ($TB \simeq 0.2$) and only a moderate overlap in frequency ($F/B \simeq 2$). This is due to the choice of a single-user detector (which cannot cope with ICI). On the other hand, a multi-user detector would allow for a more relevant packing also in frequency domain, providing a higher SE at the expense of a higher complexity.

In principle, the TFP optimization procedure described here can be applied also to a realistic fiber-optic channel, as the AIR definition (3), its properties, and the simulation-based method for its computation [18] are valid for *any* channel. The only requirement is that of computing the output sequence $\{\mathbf{y}_k\}$ for the desired real channel (e.g., through the split-step Fourier method). This, however, significantly increases the computation time required to estimate a single AIR value and makes the optimization procedure cumbersome. For this reason, we decided to optimize the system in the absence of nonlinear effects, and then tested the obtained suboptimum configuration (the one in Fig. 2) over a realistic link. A numerical estimate of the achievable SE with the suboptimum configuration over the realistic link (including nonlinear effects) is reported in Section VI (Fig. 12) and compared to experimental results.

The achievable SE obtained with this design procedure can be practically approached by employing properly designed codes. When the TFP technique is adopted, and thus ISI is intentionally introduced, codes designed for the AWGN channel no longer perform satisfactorily. So a redesign is required. We designed proper LDPC codes specifically tailored for the ISI channels resulting from the adoption of the TFP technique. The adopted procedure is based on two steps. The heuristic technique for the optimization of the degree distributions of the LDPC variable and check nodes proposed in [23] is first adopted. This technique consists in a curve fitting on extrinsic information transfer (EXIT) charts, is based on a Gaussian assumption on all messages involved in the iterative process, and is much simpler than other optimization techniques, such as density evolution, which require intensive computational efforts. The parameters of the designed codes are reported in Table I where r denotes the rate of the code and the degree distributions of variable and check nodes are provided by giving the fraction a_i ($\sum_i a_i = 1$) of degree i nodes. In any case, the codeword length is $N = 64800$.

Once the degree distributions of the LDPC variable and check nodes have been designed, the parity check matrix of an LDPC code with those degree distributions is built through the very effective PEG algorithm [24], [25], which allows to design an LDPC code whose underlying Tanner graph has a large girth. The BER curves for uncoded QPSK transmission and for the designed LDPC codes (independent encoding of the in-phase and quadrature components of each polarization) obtained through numerical simulations for the back-to-back system with the TFP configuration adopted in the experimental setup (constrained optimum at 40 Gbd and frequency spacing $F = 20$ GHz) are reported in Fig. 3. With this TFP configuration, the 8/9 LDPC code requires $E_b/N_0 \simeq 9.3$ dB and

⁵This means that the TFP system is optimized in the back-to-back configuration. However, in a practical implementation, most impairments (e.g. chromatic and polarization mode dispersion) are compensated for by DSP, as explained in Section IV, and do not change the nature of the channel. The other impairments, such as fiber nonlinearity, are responsible for a decrease of the AIR with respect to the AWGN channel. These impairments can be simply included in the computation of the achievable SE and in the optimization of the TFP system, as briefly discussed later and detailed in [8].

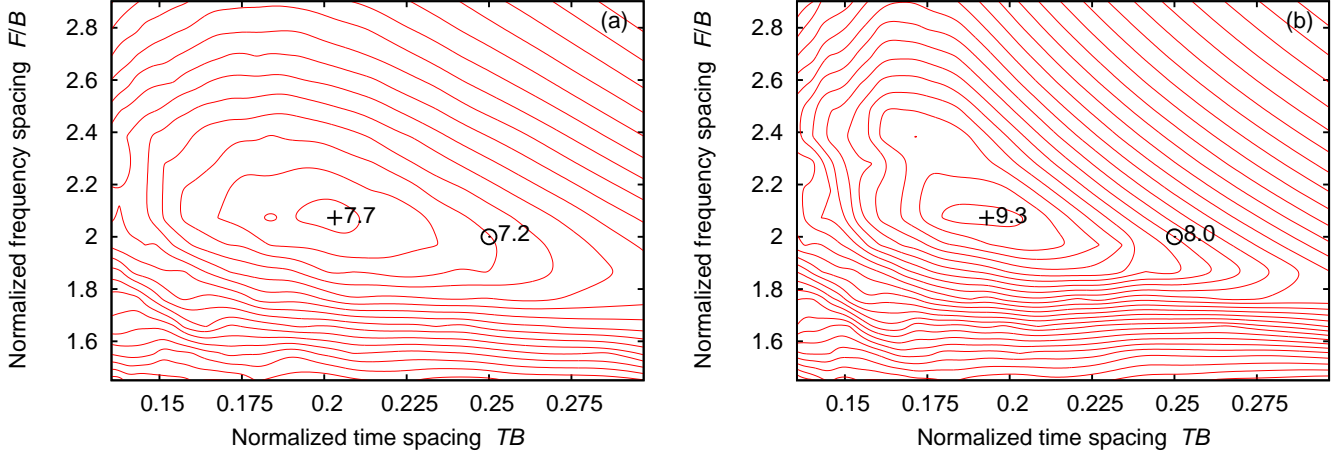


Figure 2. Contour plots of the achievable SE (obtained by numerical simulations and shown with increments of 0.2) as a function of the normalized time and frequency spacing for DP-QPSK modulation on the AWGN channel for: (a) $E_b/N_0 = 7.5$ dB; (b) $E_b/N_0 = 22.5$ dB. The maximum value (+) and the value obtained with one of the configurations adopted in the experimental setup (⊕) are also reported at the corresponding coordinates.

Table I
CODE RATES AND DEGREE DISTRIBUTIONS OF THE DESIGNED LDPC CODES.

r	variable node distribution	check node distribution
2/3	$a_2 = 0.333318$ $a_3 = 0.6$ $a_{13} = 0.0666821$	$a_9 = 0.000277778$ $a_{10} = 0.998935$ $a_{11} = 0.000787037$
3/4	$a_2 = 0.249985$ $a_3 = 0.666682$ $a_{12} = 0.0833333$	$a_{13} = 0.000679012$ $a_{14} = 0.99858$ $a_{15} = 0.000740741$
4/5	$a_2 = 0.2$ $a_3 = 0.699985$ $a_{11} = 0.100015$	$a_{18} = 0.999383$ $a_{19} = 0.000617284$
5/6	$a_1 = 1.54321 \cdot 10^{-5}$ $a_2 = 0.166651$ $a_3 = 0.75$ $a_{13} = 0.0833333$	$a_{21} = 9.25926 \cdot 10^{-5}$ $a_{22} = 0.999907$
8/9	$a_2 = 0.111096$ $a_3 = 0.777793$ $a_4 = 0.111111$	$a_{27} = 0.999861$ $a_{28} = 0.000138889$

provides an SE of about 7.1 bit/s/Hz. Thus, we can compare it with Fig. 2(a), which shows that approximately the same SE (7.2 bit/s/Hz) is theoretically achievable at $E_b/N_0 = 7.5$ dB. This means that the designed code over the (back-to-back) TFP channel has a penalty of less than 2 dB with respect to the theoretical limit provided by the AIR in (4). The gap between the actual rates achieved by the designed codes over the fiber-optic channel (including nonlinear effects) and the AIR over the same channel is numerically investigated in Section VI (Fig. 12) and is between 2 and 3 dB for all the codes. Detection of this kind of codes is typically characterized by the presence of error floors at high SNRs. In our simulations, we transmitted up to 10000 codewords without observing any floor, meaning that error floors, if present, are probably located at a BER lower than 10^{-8} . In any case, outer hard-decision external codes with very low overhead can be employed to correct the residual errors and remove the floor. For instance, in the DVB-S2 standard, where LDPC codes with same length and rates as in Tab. I are adopted, outer BCH codes with less than 0.4% overhead are used to correct from 8 to 12 residual errors (depending on the rate) per codeword [26]. In this case, an interleaver might be needed between the inner LDPC and outer BCH code, increasing the latency of the system.

IV. SYSTEM IMPLEMENTATION

A fiber-optic system based on the TFP approach can be implemented by using the same hardware configuration typically used for WDM systems based on coherent detection [27]. A significant difference is in the DSP algorithms actually

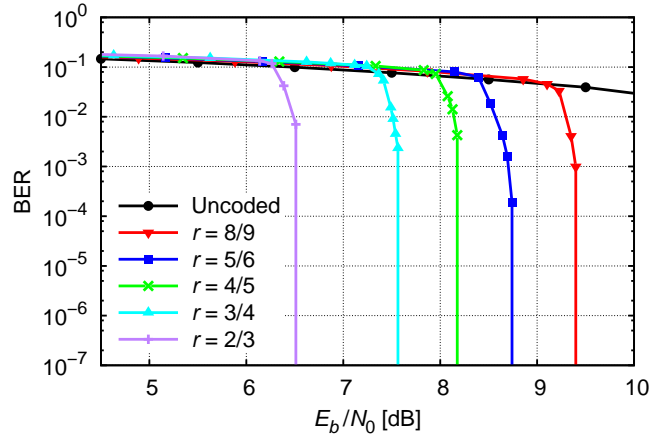


Figure 3. Back-to-back BER for uncoded transmission and for the designed LDPC codes, obtained through numerical simulations with the TFP configuration adopted in the experimental setup (40 Gbd configuration).

required at the receiver. Moreover, some care should be taken to ensure that the transmitted signal is linearly modulated as in (1). In this section, we will refer to the transmitter and receiver implementation schemes shown in Fig. 4, focusing on those elements which are peculiar to the TFP implementation. Practical details about the experimental setup actually employed in the experimental demonstration will be given in Section V.

Since the system employs single-user detectors, an independent transmitter and receiver pair is used per each

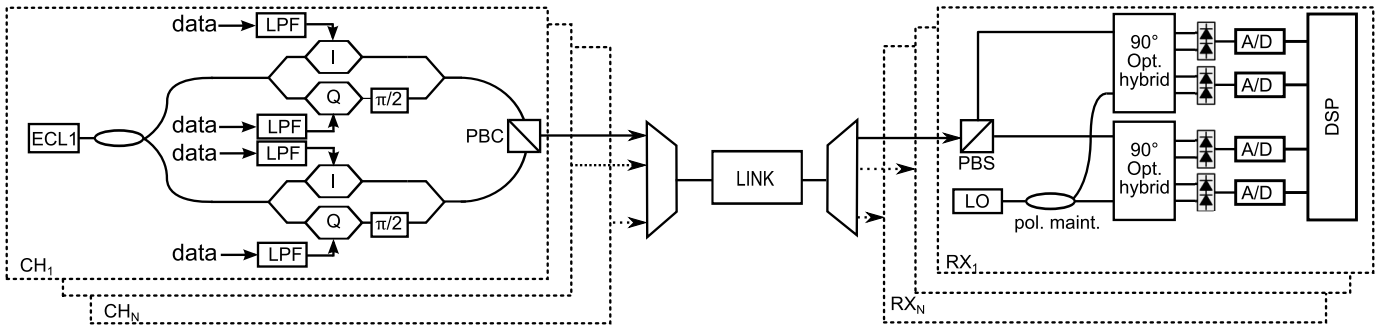


Figure 4. Transmitter and receiver schemes of a TFP system employing DP-QPSK modulation.

optical carrier. Each optical carrier is thus generated at the desired wavelength (e.g., by an external-cavity laser (ECL)), modulated, optically multiplexed with the other modulated carriers, transmitted through the optical link, extracted by an optical demultiplexer, and independently detected. In each transmitter, the in-phase and quadrature components of two orthogonal states of polarization are independently and linearly modulated by a pair of nested Mach-Zehnder modulators (MZMs). In principle, the desired pulse shape $p(t)$ can be obtained either operating on the electrical signals that drive the modulator (through a low-pass filter (LPF), as actually shown in the scheme of Fig. 4) or on the optical signal after the modulator (through an optical band-pass filter), provided that the overall equivalent low-pass impulse response of the transmitter (driver, modulator, electrical filter and/or optical filter) is $p(t)$ and that linearity of the modulator is preserved by employing a driving voltage significantly lower than the modulator half-wave voltage V_{π} . A comparison of the performance obtained by optical or electrical filtering when employing different driving voltages is presented in [28]. An alternative modulation scheme, where linear modulation (1) is obtained by operating the MZM at its maximum driving voltage (to reduce its insertion loss), may also be devised. For instance, by using an additional MZM as a pulse carver and employing optical filtering to obtain the desired pulse shape $p(t)$ and BT product [5], [8], the nonlinearity of the MZM affects only (and slightly) the overall pulse shape $p(t)$, but does not introduce nonlinear ISI. In this scheme, however, the insertion loss saved by increasing the MZM driving voltage is replaced by the additional loss introduced by the pulse carver and optical filter. Finally, a possible implementation based on an arrayed waveguide grating device that filters and multiplexes all the frequency subchannels in the optical domain has been proposed in [29]. In this work, we consider a modulation scheme based on a single MZM (driven at low voltage) and analogue electrical filtering which, at the present, seems to be the most practical choice in terms of cost and complexity. Moreover, as discussed in Section III, the choice of $p(t)$ is not critical and a reasonably good performance can be obtained by employing available analogue low-pass filters, as shown in Fig. 2.

At the receiver side, each optical carrier is demodulated by employing a phase- and polarization-diversity coherent

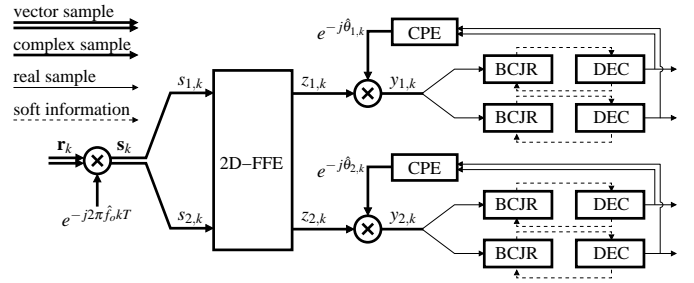


Figure 5. Digital signal processing scheme.

detection scheme. After optical demultiplexing, each carrier is split into two orthogonal states of polarizations, which are then separately combined with the optical field of a local oscillator (LO) laser in a 2×4 90° optical hybrid and detected with two pairs of balanced photodetectors. The four resulting electrical signals (the in-phase and quadrature components of each state of polarization) are then sampled by an A/D converter with a bandwidth $B_s \geq B$, where B is the (low-pass) bandwidth of the shaping pulse $p(t)$, and a sampling rate $R_s \geq 2B_s$. The remaining part of receiver processing is digitally implemented according to the scheme depicted in Fig. 5, assuming a sampling rate $R_s = 1/T$. Note that, since TFP is employed, the required bandwidth and sampling rate are typically lower than $1/(2T)$ and $1/T$, respectively, and digital upsampling can be employed to achieve the sampling rate $R_s = 1/T$ required for symbol-time processing, without any performance degradation. The k -th received column vector of samples $\mathbf{r}_k = (r_{1,k}, r_{2,k})^T$ (one complex sample per state of polarization) is first processed to compensate for the presence of any large and slowly varying frequency offset f_o between the transmit and receive lasers. The estimate \hat{f}_o is obtained during the training phase (on a known training sequence) by employing the frequency estimation algorithm described in [30], and then slowly updated based on decisions. Compensated samples $\mathbf{s}_k = \mathbf{r}_k e^{-j2\pi\hat{f}_0kT}$ are then processed by an adaptive 2-D N_c -tap synchronous feed-forward equalizer (FFE) that compensates for linear propagation impairments, such as group-velocity dispersion (GVD), polarization rotations, and polarization-mode dispersion (PMD), and completes (as explained later) the implementation of the matched filter. Symbol timing synchronization is also performed by

the adaptive equalizer. As the system performance is nearly independent of the clock phase when the period of the equalizer transfer matrix ($1/T$ when a synchronous equalizer is employed) is larger than twice the low-pass bandwidth of the signal (about $1/4T$ in our TFP implementation, as shown in Fig. 2), a simple feedback signal for the clock rate can be obtained by monitoring the dynamics of the equalizer coefficients, which reflect the drift of the clock phase due to an error of the clock rate [31]. However, in the experimental implementation of Section V, in which signal samples are collected in blocks of 1 million per quadrature, the drift of the clock phase is negligible and no clock recovery is employed. At the output of the equalizer, the components $z_{1,k}$ and $z_{2,k}$ of the equalized samples \mathbf{z}_k are then separated and independently processed. For each component, decision-directed carrier phase estimation (CPE) based on the Tikhonov parametrization algorithm [32] is employed to cope with the laser phase noise⁶. Finally, the in-phase and quadrature components of the compensated samples $y_{1,k} = z_{1,k}e^{-j\hat{\theta}_{1,k}}$ and $y_{2,k} = z_{2,k}e^{-j\hat{\theta}_{2,k}}$ are separated and sent to four parallel $2L_T$ -state BCJR detectors [21], followed by four LDPC decoders. The BCJR detectors and LDPC decoders iteratively exchange information to achieve MAP detection according to the turbo principle [33]. At each iteration, as new (more accurate) preliminary decisions are available from the decoders, the CPEs update the phase estimates $\hat{\theta}_{1,k}$ and $\hat{\theta}_{2,k}$ and a new set of compensated samples $y_{1,k}$ and $y_{2,k}$ is fed to the BCJR detectors. At the first iteration, as preliminary decisions are not available, the CPEs exploit pilot symbols (evenly inserted in the transmitted sequence at rate r_p) to provide a rough initial estimate of the phase and make the iterative process bootstrap.

The equalizer should be configured to make the low-pass equivalent model of the system as close as possible to the ideal scheme considered in Fig. 1. Considering that the amplified-spontaneous-emission (ASE) noise accumulated during propagation can be modeled, with good approximation, as independent AWGN on each polarization at the input (or, equivalently, at the output) of the fiber link, and that the transfer matrix of the link $\mathbf{H}_f(f)$ (in the linear regime) is unitary, i.e., $\mathbf{H}_f(f)^{-1} = \mathbf{H}_f(f)^\dagger$, the required transfer matrix

of the 2D-FFE equalizer should be⁷

$$\mathbf{H}_{\text{eq}}(f) = \mathbf{H}_f(f)^\dagger P(f)^*/H_{\text{fe}}(f) \quad (5)$$

where $H_{\text{fe}}(f)$ is the low-pass equivalent transfer function of the optoelectronic front-end (optical filter, photodetector, and A/D converter). In this case, the corresponding overall channel transfer matrix would be $\mathbf{H}(f) = |P(f)|^2\mathbf{I}$, with \mathbf{I} the 2×2 identity matrix, independently of the actual transfer matrix of the fiber. A naive evaluation of (5) for the system at hand requires an accurate characterization of transmitter and receiver front-end, and an adaptive estimate of the fiber transfer matrix $\mathbf{H}_f(f)$. Here, instead, taking inspiration from [19], an algorithm has been devised that configures the equalizer according to (5), without requiring a separate knowledge of $\mathbf{H}_f(f)$, $P(f)$, and $H_{\text{fe}}(f)$. Denoting by \mathbf{C}_i the 2×2 matrix of coefficients of the i -th tap of the equalizer, the equalized samples are

$$\mathbf{z}_k = \sum_{i=0}^{N_e-1} \mathbf{C}_i \mathbf{s}_{k-i} \quad (6)$$

Denoting by \mathbf{x}_k the k -th column vector of transmitted symbols, by \mathbf{h}_i the column vector of the two i -th coefficients of the desired (but unknown) overall impulse responses at the output of the matched filter (one per polarization), and by $\mathbf{g}_k = (e^{j\hat{\theta}_{1,k}}, e^{j\hat{\theta}_{2,k}})^T$ the column vector of the phase estimates for the k -th samples on the two polarizations, the error with respect to the desired channel response is

$$\mathbf{e}_k = \mathbf{g}_k^* \circ \mathbf{z}_k - \sum_{i=-L_T}^{L_T} \mathbf{h}_i \circ \mathbf{x}_{k-i} \quad (7)$$

where \circ denotes the Hadamard (entrywise) product and L_T is the design parameter introduced in Section III. As shown in [19], the variance of each element of (7) is minimum when the matched filter condition is met, i.e., when $\mathbf{H}_{\text{eq}}(f)H_{\text{fe}}(f)\mathbf{H}_f(f) = P^*(f)\mathbf{I}$. Given the unitarity of $\mathbf{H}_f(f)$, this is equivalent to (5) and provides the desired overall response $\mathbf{H}(f) = |P(f)|^2\mathbf{I}$. Thus, both the required equalizer coefficients and the desired channel coefficients of the Ungerboeck observation model can be simultaneously estimated by an iterative data-aided stochastic-gradient algorithm that minimizes the variance of (7). By holding \mathbf{h}_0 constant (to an arbitrary value) and forcing the symmetry condition $\mathbf{h}_{-i} = \mathbf{h}_i^*$, the update law for the equalizer coefficients and

⁶The algorithm in [32] is properly modified to use (preliminary) hard decisions (which are a particular case of soft decisions used in [32]) and to account for ISI by filtering the preliminary decisions with the overall impulse response of the channel, estimated as explained later. The algorithm is also modified to extract hard (rather than soft) estimates $\hat{\theta}_{1,k}$ and $\hat{\theta}_{2,k}$ of the carrier phase for the two polarization components. Considering the notation in [32], and in particular the factor graph in Fig. 2 of [32], the product of the incoming messages $p_d(\theta_k)$, $p_f(\theta_k)$, $p_b(\theta_k)$ to variable node θ_k is proportional to the a posteriori probability density function of the carrier phase θ_k at discrete time k given the received sequence. Its argmax is thus the MAP estimate $\hat{\theta}_k$ of θ_k (for either of the two polarizations). In particular, having the a posteriori probability density function of θ_k a Tikhonov distribution, the MAP estimate we are looking for equals the argument of the complex parameter of this distribution.

⁷In the following, $(\cdot)^*$ denotes conjugate and $(\cdot)^\dagger$ transpose conjugate. For the sake of simplicity, we assume that the analog components at transmitter and receiver are perfectly balanced among the four tributaries, such that they can be modeled by scalar transfer functions. Moreover, we neglect nonlinear effects, polarization dependent loss (PDL), and optical filters along the optical link, such that fiber propagation can be modeled by a unitary transfer matrix. In deriving the algorithm described later, some of these assumptions could be safely removed (e.g., including in-line optical filters), as the proposed approach works even in the presence of colored noise [19]. On the other hand, in the presence of PDL, hardware imbalances, and nonlinear effects, the optimality of the proposed approach should be carefully investigated and a separate processing of the in-phase and quadrature components (by a four-dimensional real-coefficient equalizer) would be required. Nevertheless, as shown by the experimental results of Section V, the proposed algorithm still works satisfactorily in the presence of the aforementioned effects (which are naturally present in the experimental setup).

the estimated channel coefficients are, respectively

$$\mathbf{C}_i^{(k+1)} = \mathbf{C}_i^{(k)} - \alpha_c (\mathbf{g}_k \circ \mathbf{e}_k) \mathbf{s}_{k-i}^\dagger, \quad 0 \leq i \leq N_c - 1 \quad (8)$$

$$\mathbf{h}_i^{(k+1)} = \mathbf{h}_i^{(k)} + \alpha_h (\mathbf{e}_k \circ \mathbf{x}_{k-i}^* + \mathbf{e}_k^* \circ \mathbf{x}_{k+i}), \quad 1 \leq i \leq L_T \quad (9)$$

where α_c and α_h are the step-size gains. For an accurate estimate of the whole channel response, L_T should be taken at least equal to L , where $2L + 1$ is the overall channel memory. However, by choosing a lower L_T , the equalizer forces ISI to zero beyond the previous and past L_T symbols, which provides a better performance when combining the equalizer with the 2^{L_T} -state BCJR detectors [19]. Updates (8) and (9) require knowledge of the transmitted symbols. While the equalizer coefficients need to be continuously updated to track variations of the fiber-optic channel, coefficients $\{\mathbf{h}_i\}$ of the overall channel response do not change with time and can be estimated only once when setting up the link, unless the link transfer matrix is not unitary (e.g., due to PDL). The initial convergence of the algorithm can be guaranteed by the use of a known training sequence, while a slow tracking of the fiber channel can be achieved by updating only the equalizer coefficients according to (8), possibly at a much lower rate than $1/T$ and with a significant delay⁸. This allows to use pilot symbols and/or to replace transmitted symbols with final decisions (after successful decoding of the whole codeword), with a negligible impact on information rate and performance.

The computation of the channel metrics for the BCJR algorithm requires knowledge of the channel coefficients $\{\mathbf{h}_i\}$ and of the noise variance. Thus, once estimated by (9), channel coefficients are passed to the BCJR processing blocks together with an estimate of the variance of (7).

V. EXPERIMENTAL DEMONSTRATION

Fig. 6 shows the experimental setup employed for the practical implementation of the TFP system and for the transmission experiments. Five external-cavity lasers (ECL) are grouped into two sets (odd and even channels), which are separately modulated by means of two integrated nested Mach-Zehnder modulators (IQ-MZM). Bandwidth, rate, and spacing of the five TFP channels are optimized (under some constraints posed by the available hardware) according to the design procedure described in Section III to maximize the achievable SE with the desired detector complexity. In particular, the optical carrier spacing is set to $F = 20$ GHz and the binary electrical signals that drive the in-phase (I) and quadrature (Q) port of each IQ-MZM are modulated at a rate $R = 1/T = 40$ GBd and filtered by a ninth-order Chebyshev low-pass filter (LPF) with a 3dB-bandwidth $B = 10$ GHz⁹. The peak-to-peak modulation voltage is set to $V_{pp} = 1.5$ V, while the half-wave voltage of each MZM is $V_\pi = 2.8$ V.

⁸As variations of the fiber-optic channel typically take place on a time scale of milliseconds, the channel remains approximately constant over many consecutive codewords.

⁹This configuration is twice more ‘‘packed’’ than allowed by the Nyquist limit: its time-frequency spacing product is $FT = 0.5$, meaning that two QPSK symbols are transmitted per second per Hertz per polarization.

For the same fixed bandwidth and spacing, lower transmission rates of 35 and 30 GBd are also considered¹⁰. Polarization multiplexing is emulated by means of a 50/50 beam splitter, an optical delay line, and a polarization beam combiner (PBC). Each I and Q component is modulated by a sequence of random information bits, which are independently encoded according to one of the LDPC codes reported in Tab. I. Odd and even channels are then combined by means of a 2×1 optical coupler (OC). The optical spectrum of the transmitted TFP superchannel (at the input of the recirculating loop) is depicted in Fig. 7.

At the receiver side, one of the five TFP channels is detected by employing coherent phase- and polarization-diversity detection and setting the local oscillator (LO) at the nominal wavelength of the selected channel. The received optical signal is mixed with the LO through a polarization-diversity 90° hybrid optical coupler, whose outputs are sent to four pairs of balanced photodiodes. The four photodetected signals are sampled and digitized through a 20 GHz 50 GSa/s real-time oscilloscope in separate blocks of one million samples at a time, corresponding to about 12 codewords (at 40 GBd) per each quadrature component. After digital resampling at rate $1/T$ (one sample per symbol), each block is processed off-line according to the scheme of Fig. 5, with $N_c = 23$ equalizer taps and $L_T = 3$ (a truncated channel memory of $2L_T + 1 = 7$ symbols, which requires an 8-state BCJR detector). The first received codeword of each block (on each quadrature component) is used as a training sequence for the convergence of the DSP algorithms (initial estimate of the frequency offset \hat{f}_0 , equalizer coefficients \mathbf{C}_i , and channel coefficients \mathbf{h}_i), while the others are effectively employed to measure system performance. This is not considered in the computation of the SE as, in a real system, the training sequence would be transmitted only once. After decoding of each codeword, the equalizer coefficients are then slowly updated (one update each 500 decoded symbols) according to (8) by employing decisions. Pilot symbols at rate $r_p = 1/400$ are finally employed (and accounted for in the SE computation) to make the iterative decoding process (CPE, BCJR detection, and LDPC decoding) bootstrap. A maximum of 20 turbo iterations for the CPE, BCJR, and LDPC decoder is considered.

Bit-error rate (BER) measurements are performed off-line by averaging over a total of about 500 randomly selected codewords (of length 64800). Although this result should set a limit for BER measurements at about 10^{-6} , it is known that LDPC error floors entails bit errors in bursts, preventing the reliable measurement of such low BER. However, the design of LDPC codes with low error floors falls outside the scope of our work and we conjecture, based on extensive computer simulations and measurement campaigns [34], that the employed codes do not present floors for packet error rate higher than 10^{-7} . This sets a limit for the minimum measurable BER at about 10^{-7} , and for reliable BER measurements at about 10^{-6} . Transmission is considered to be error-free when

¹⁰If the bandwidth of the terminal filters is not proportionally reduced, the LDPC codes are slightly suboptimal.

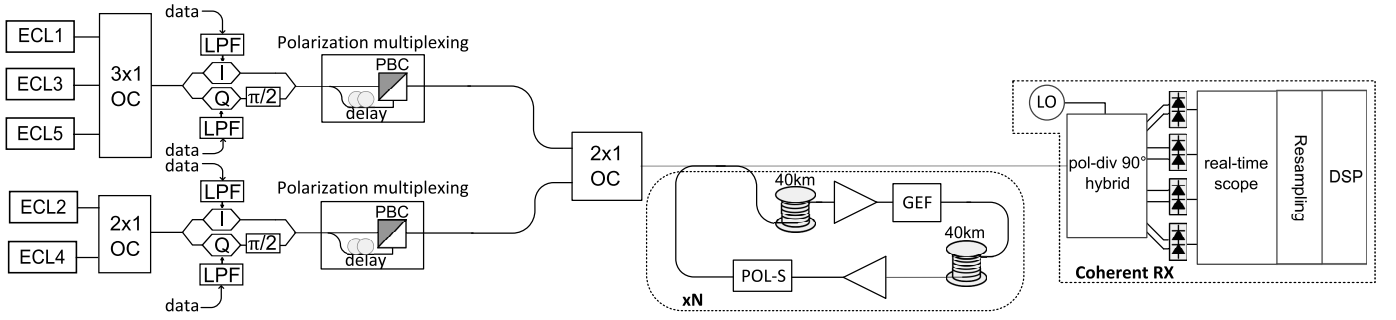


Figure 6. Experimental setup.

all the information bits are correctly decoded at the receiver, which means, in fact, $\text{BER} < 10^{-6}$ with high probability. As discussed in Section III, detection of the adopted LDPC codes is characterized by the presence of possible error floors at $\text{BER} < 10^{-8}$ (a too low value to be observed either experimentally or in standard simulations), which can be practically removed by concatenating outer hard-decision BCH codes with small additional overhead ($< 0.4\%$) and complexity [26]. We account for this fact by virtually including a BCH code with rate $r_{\text{BCH}} = 0.996$ (0.4% redundancy) in the computation of the experimentally achieved SE, which is therefore defined as the actual amount of information that is reliably transmitted (error-free within measurement accuracy) per unit time and bandwidth once the overhead due to the LDPC code, outer BCH code (virtually present), and pilot symbols is removed

$$\tilde{\eta} \triangleq \frac{4r_{\text{LDPC}}r_{\text{BCH}}(1-r_p)}{FT} \leq \hat{\eta}_{\text{max}}. \quad (10)$$

Depending on the available E_b/N_0 and on the presence of uncompensated transmission impairments, different code rates r_{LDPC} are required to obtain reliable transmission. The transmission system can thus be adapted to finely adjust the information rate to the channel conditions (accumulated noise and propagation penalties) by changing r_{LDPC} (selected among the values available in Tab. I) while keeping the transmission rate $1/T$ and channel spacing F constant. A wider tuning of the SE is finally obtained by changing also the transmission rate. In particular, rates of 40, 35, and 30 GBd are considered. The difference between the experimentally achieved SE (10) and the theoretically achievable SE (4) depends on the performance (and available rate granularity) of the designed LDPC codes and on the presence of any additional impairment unaccounted for in this design procedure (e.g., modulator imperfections, nonlinearity, etc.).

Long-distance transmission is emulated by using a recirculating loop, composed of two 40 km long spans of standard single mode fiber, two optical amplifiers, a polarization scrambler (POL-S), and a gain equalizer filter (GEF). The total dispersion accumulated during propagation through the recirculating loop is compensated by a static frequency-domain equalizer, placed in front of the 2D-FFE equalizer and configured according to the selected link length.

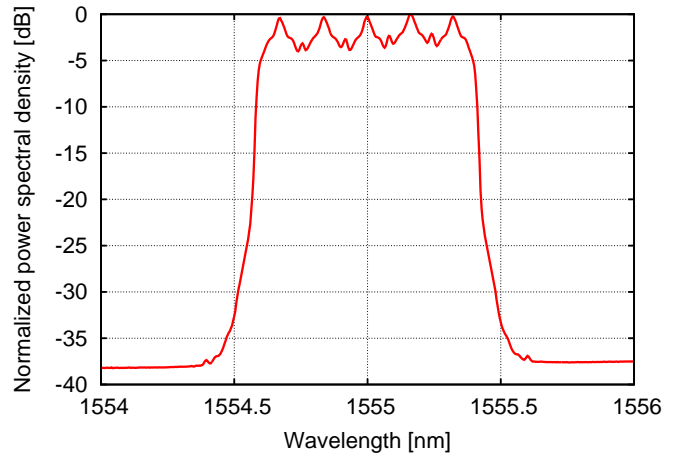


Figure 7. Normalized optical spectrum of the TFP superchannel at the input of the recirculating loop.

A. Back to back measurements

The back-to-back performance of the system is investigated by bypassing the recirculating loop and measuring only the BER of the central channel. In order to experimentally verify the TFP optimization performed numerically in Section III, signals at different baud rates are generated and coded with different code rates. Fig. 8 shows the measured BER values as a function of E_b/N_0 (obtained by measuring the OSNR through an optical spectrum analyzer and using the relation $E_b/N_0 = 2B_{\text{ref}}\text{OSNR}/R_b$) for a 40 GBd transmission and some of the LDPC codes reported in Tab. I. Compared to simulation results in Fig. 3, the experimental penalty is about 2 dB for the 3/4 LDPC code and increases up to more than 3 dB for the 8/9 code. This can be explained by considering that the measured E_b/N_0 ratio reported on the x-axis accounts only for optical noise. Thus, we expect an experimental penalty due to electrical noise (and other receiver imperfections) that becomes more relevant as the measured E_b/N_0 increases (i.e., the amount of optical noise decreases). Fig. 9 shows the achieved SE, defined according to (10), for 30, 35, and 40 GBd transmission. In practice, Fig. 9 reports, for each code rate and baud rate, the achieved SE and the corresponding minimum required E_b/N_0 ratio to obtain reliable transmission (where the BER curves in Fig. 8 suddenly drop to zero). As predicted by Fig. 2, the highest SE is achieved at 40 GBd transmission

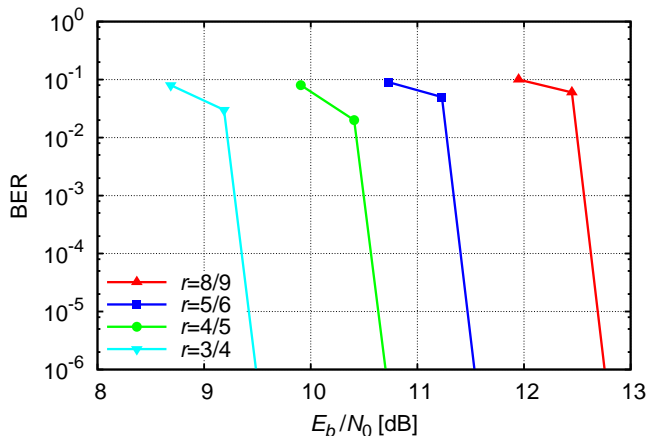


Figure 8. Experimental back-to-back performance of the TFP system (only central channel): BER with the 40 GBd DP-QPSK configuration and different code rates.

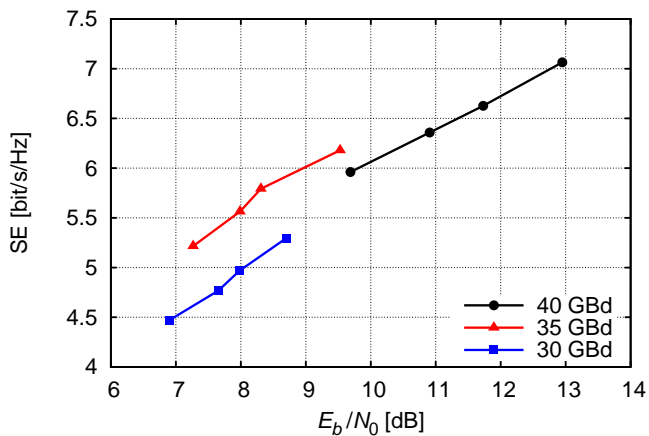


Figure 9. Experimental back-to-back performance of the TFP system (only central channel): achieved SE with the 40 GBd, 35 GBd, and 30 GBd DP-QPSK configuration.

(and could be possibly increased by further increasing the transmission rate up to 50 GBd, though we could not verify it due to limitations of the available hardware). However, for low SNRs, a slightly better efficiency can be obtained at 35 GBd.

B. Transmission experiments

Transmission experiments are performed by properly setting the number of rounds that the signal travels through the recirculating loop in Fig. 6. The launch power is optimized to obtain the best trade-off between noise and nonlinear propagation effects. For the sake of simplicity, it is assumed that the optimal launch power is independent of the transmission distance and code rate. The optimization is performed by setting the same power for the five channels and measuring the performance of the third (central) one, which is the most affected by inter-channel nonlinearity. Fig. 10 shows the maximum achievable transmission distance as a function of the launch power, for either 30 or 40 GBd transmission and a fixed SE $\bar{\eta} \simeq 5.3$ bit/s/Hz (obtained with code rates

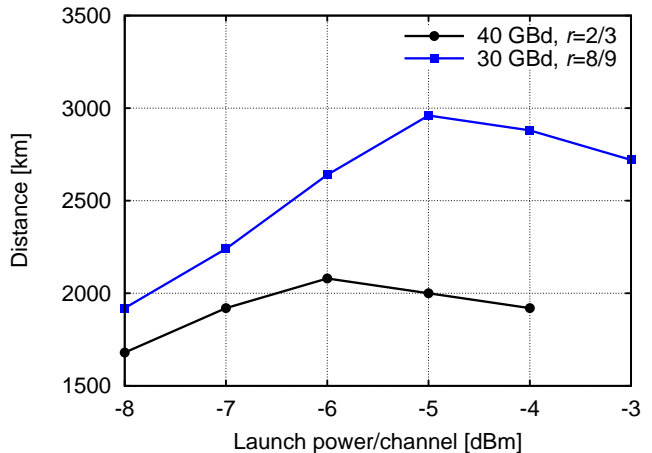


Figure 10. Optimization of the launch power: reached distance vs launch power at a fixed SE $\bar{\eta} \simeq 5.3$ bit/s/Hz.

of 8/9 and 2/3, respectively). A slightly different result is obtained for 30 GBd and 40 GBd transmission, the optimum launch power being -5 and -6 dBm per channel, respectively. However, in the following measurements, the same launch power of -5 dBm per channel is used for any transmission rate. Once the launch power has been set, the maximum achieved SE $\bar{\eta}$ —defined in (10) and obtained by selecting the highest code rate (among the available ones reported in Tab. I) guaranteeing error-free transmission—is measured as a function of the transmission distance for a transmission rate of 30, 35, and 40 GBd. Fig. 11 shows the results for each of the five TFP channels (symbols) as well as for the whole super-channel (lines, corresponding to the worst-performing channel). Due to inter-channel nonlinearity (as $F = 2B$, linear crosstalk among channels is practically negligible), the central channel is typically the worst performing, while the outer channels are the best performing. This is more evident at higher transmission rates. At short distances, i.e. at high OSNRs, the achieved SE is much higher (about 7.1 bit/s/Hz at 400 km) than the theoretical limit of 4 bit/s/Hz achievable by Nyquist-WDM transmission with same DP-QPSK modulation format, and remains higher up to almost 6000 km. Moreover, the SE can be adapted to the propagation conditions by simply changing the code rate or, for significant OSNR variations, the amount of packing (i.e., the baud rate $1/T$ or, equivalently, the bandwidth B and the frequency spacing F), without changing the modulation format and transceiver hardware.

VI. DISCUSSION

As a recent and not yet fully mature technique, TFP can be still improved in terms of performance and complexity. In this sense, the implementation proposed in this work is intended to demonstrate the technical feasibility and good performance of TFP and should not be considered as the ultimate TFP solution. In fact, there are several options to improve the performance (SE vs. distance) of the proposed TFP transmission technique beyond that achieved in our experiments. In the first place, we consider some improvements that, being related to the design, optimization, or implementation of the system, do

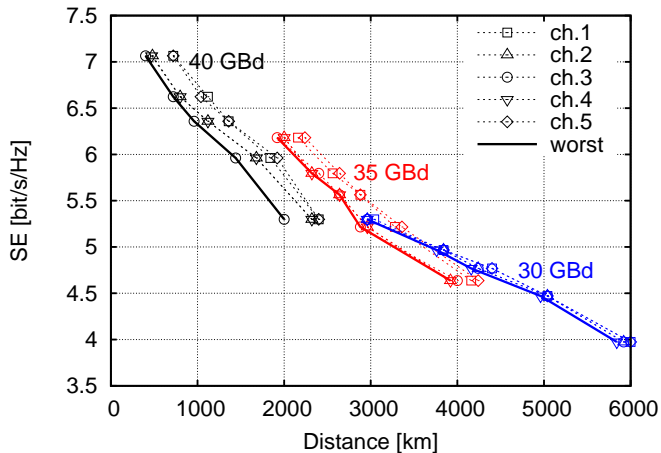


Figure 11. Experimentally achieved SE (all the TFP channels) vs reached distance with the 40 GBd, 35 GBd, and 30 GBd DP-QPSK configuration.

not affect its complexity. As indicated in Fig. 2, due to some limitations in the available hardware, the adopted configuration is not exactly the optimum one. In fact, according to numerical simulations, the optimum configuration provides from 0.5 to 1 bit/s/Hz of improvement of the achievable SE (for low and high OSNRs, respectively) compared to the suboptimum configuration actually employed in the experimental setup. Moreover, as the optimization of Fig. 2 refers to an AWGN channel, a more accurate optimization could be sought by accounting also for nonlinear effects through approximate channel models, time-consuming simulations, or directly optimizing the experimental setup through extensive measurements (in increasing order of accuracy and required time). A non-negligible improvement should be achievable, still without increasing the system complexity, also by removing possible imperfections in the experimental setup (e.g. unbalance between I/Q components or polarizations at the modulator or at the optoelectronic front-end). This could provide up to 2 dB of improvement in the required SNR, as suggested by the comparison between Fig. 3 and 8. A similar improvement could be achieved also by designing better LDPC codes (with a lower distance from the Shannon limit), as discussed in Section III. Such an improvement in the required SNR would then translate into an almost proportional improvement in terms of maximum transmission distance. This is shown in Fig. 12, which compares the achieved SE (10) measured in the experimental setup (the 40 GBd configuration), the achieved SE (10) estimated through numerical simulations (including nonlinear effects but without accounting for TX or RX imperfections), and the achievable SE (4) (for the best possible code) over the nonlinear optical channel. The latter is estimated through numerical simulations as in [8], in which the output samples $\mathbf{y}^{(0)}$ in (3) are obtained by propagating the input samples $\mathbf{x}^{(0)}$ through the nonlinear optical fiber link by means of the SSFM algorithm, such that the expectation in (3) is evaluated according to the actual sample distribution over the nonlinear channel and represents the AIR over that channel. The difference between the first two curves (experiments and simulations) is due to the aforementioned imperfections of the

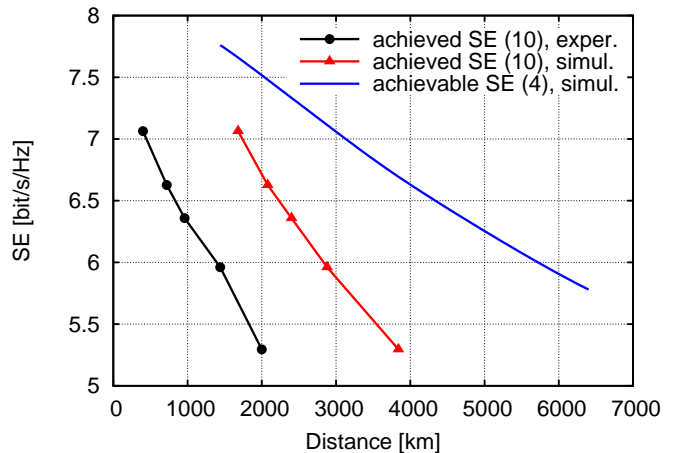


Figure 12. Comparison among the SE achieved with the experimental setup, the SE achieved in numerical simulations, and the theoretically achievable SE.

experimental setup, which are not considered in the numerical simulations and could be possibly removed. Moreover, for high OSNR values (i.e., at short distances), electronic noise and quantization effects at the receiver (not included in the simulations) become relevant with respect to optical noise and causes an additional penalty with respect to numerical simulations. This explains why the difference between the two curves (in dBs along the x-axis) is not constant and increases at short distances. Finally, the difference between the last two curves (achieved and achievable SE) depends on the actual performance of the designed LDPC codes compared to the ultimate limit provided by the information theoretical analysis.

In the second place, a significant improvement can be obtained at the expense of an additional DSP complexity. For instance, by modifying the detection strategy to account for a longer ISI (e.g. increasing the number of trellis states or considering channel shortening techniques [35], as described in [8]) and/or also for ICI (multi-user detection), pulses can be more densely packed, achieving a higher SE. Finally, the DSP implemented in the experimental setup does not include any nonlinearity mitigation strategy, which could be adopted to improve the overall performance. For instance, as confirmed by some preliminary results, the low-complexity digital backpropagation strategy proposed in [36] can be easily integrated in the DSP (replacing the static frequency-domain equalizer for dispersion compensation) to mitigate intra-channel nonlinearity and extend the reach. This subject is however outside the scope of the paper and is left for a future investigation.

Due to possible improvements and ongoing research, an accurate and comprehensive comparison with more conventional (and mature) techniques (e.g., Nyquist-WDM) is not yet available. A numerical comparison between TFP and Nyquist-WDM performance can be found in [8], where it is shown that TFP can achieve higher SE values than high-order modulation Nyquist-WDM over realistic long-haul systems. In terms of peak-to-average power ratio (PAR), it is known that non-

orthogonal signaling (FTN or TFP) has a higher PAR than orthogonal signaling employing the same (QPSK) symbol alphabet, in effect inducing a sort of “higher-order constellation” which foils the beneficial effect that a constant-envelope modulation has in terms of robustness to nonlinear effects. The effect of PAR on nonlinearity becomes, however, almost negligible in dispersion-unmanaged systems with relevant span losses [37]. Moreover, as shown in [8], TFP outperforms high-order Nyquist-WDM especially in the presence of nonlinear effects. The actual PAR is not relevant even in terms of the resolution of the required A/D or D/A converters. In fact, no D/A is employed to generate the TFP signal. On the other hand, received samples in dispersion-unmanaged systems are always (with high accuracy) Gaussian distributed because of the accumulated dispersion [38], such that the PAR of the received signal is independent of the modulation format. TFP offers advantages also at a network level, as it provides high SE and flexibility (e.g., reach adaptation and filter configuration) without requiring transponders supporting multiple modulation formats [7]. In terms of complexity, TFP has the advantage of a simpler transmitter architecture (e.g., only two-level driving signals are needed to control the modulator; no DSP and D/A conversion are required to process the modulating signals; more relaxed constraints on the pulse shape can be considered) at the expense of a more complex DSP at the receiver (e.g., the 8-state BCJR detector employed in this work and the higher symbol rate that affects the rate of operations that algorithms operating at symbol time should perform). On the other hand, the use of a TFP DP-QPSK format allows to employ only symbol-time processing at the receiver and greatly simplifies decision-directed algorithms compared to higher-order modulation formats. This can partly compensate for the additional complexity of the BCJR detector.

VII. CONCLUSIONS

In this work, after reviewing the main theoretical aspects of the TFP approach, we have investigated its application to fiber-optic systems. The main challenges pertain to the peculiar nature of the channel (the optical fiber, impaired by linear and nonlinear propagation effects) and to the high data rates involved. We have thus discussed the implementation schemes, focusing on the main differences with respect to a conventional coherent WDM system. The only relevant difference is a modification of the DSP algorithms employed for detection. In the proposed scheme, a butterfly equalizer adaptively addresses propagation impairments and performs matched filtering, while intentional ISI due to TFP filtering is accounted for by a BCJR detector. To ensure a proper distribution of tasks between the equalizer and BCJR detector, an algorithm has been proposed that adaptively controls the equalizer and provide channel coefficients and noise variance to the BCJR detector. This makes the receiver fully adaptive, without requiring a priori knowledge of the adopted TFP configuration. Soft-decoding forward-error correction is finally employed. In particular, irregular LDPC codes with various code rates (in the range $2/3$ – $8/9$) and specifically optimized for the TFP channel have been designed to operate at low

error rates. They approach (within about 3 dB) the SE limits achievable by the proposed techniques at different SNRs. The performance of the proposed system has been tested both experimentally and by simulations, demonstrating technical feasibility and good performance. Five closely-packed DP-QPSK channels were transmitted through a recirculating loop, keeping the net SE beyond the theoretical limit of Nyquist-WDM (4 bit/s/Hz) up to 6000 km. The channel bandwidth and spacing was held fixed to 20 GHz, while the transmission rate and code rate were adapted, depending on the transmission distance, to the available OSNR. At 400 km, a net SE of more than 7 bit/s/Hz was achieved by setting the transmission rate at 40 GBd (twice faster than the Nyquist limit) and the code rate to $8/9$. The transmission distance was then gradually increased up to 6000 km, with a net SE which gradually decreased to about 4 bit/s/Hz (achieved with a 30 GBd transmission rate and a $2/3$ code rate). Both the LDPC encoder and decoder were actually included in the experimental setup, as it is advisable in the presence of soft decoding, for which the use of a numerically evaluated “pre-FEC BER threshold” may be unreliable.

In conclusion, we have demonstrated that TFP with low-level modulation (e.g., DP-QPSK) can be considered as a practical and viable alternative to high-level modulations to achieve high SEs over long-haul fiber-optic links, providing good performance and high flexibility (reach adaptation and filter configuration) with simpler transponder architectures (single modulation format, relaxed constraints on pulse shape, no DSP and D/A conversion at the transmitter).

REFERENCES

- [1] G. Bosco, V. Curri, A. Carena, P. Poggiolini, and F. Forghieri, “On the performance of Nyquist-WDM Terabit superchannels based on PM-BPSK, PM-QPSK, PM-8QAM or PM-16QAM subcarriers,” *J. Lightwave Technol.*, vol. 29, no. 1, pp. 53–61, 2011.
- [2] W. Shieh, X. Yi, and Q. Yang, “Coherent optical OFDM: has its time come?,” vol. 7, pp. 234–255, Mar. 2008.
- [3] A. Barbieri, G. Colavolpe, T. Foggi, E. Forestieri, and G. Prati, “OFDM vs. single-carrier transmission for 100 Gbps optical communication,” *J. Lightwave Tech.*, vol. 28, pp. 2537–2551, September 1 2010.
- [4] A. Barbieri, D. Fertonani, and G. Colavolpe, “Time-frequency packing for linear modulations: spectral efficiency and practical detection schemes,” *IEEE Trans. Commun.*, vol. 57, pp. 2951–2959, Oct. 2009.
- [5] G. Colavolpe, T. Foggi, A. Modenini, and A. Piemontese, “Faster-than-Nyquist and beyond: how to improve spectral efficiency by accepting interference,” *Opt. Express*, vol. 19, pp. 26600–26609, December 2011.
- [6] L. Potf, G. Meloni, G. Berrettini, F. Fresi, M. Secondini, T. Foggi, G. Colavolpe, E. Forestieri, A. D’Errico, F. Cavaliere, R. Sabella, and G. Prati, “Casting 1 Tb/s DP-QPSK communication into 200 GHz bandwidth,” in *Proc. European Conf. on Optical Commun. (ECOC’12)*, September 19–23, 2012.
- [7] N. Sambo, G. Meloni, F. Paolucci, F. Cugini, M. Secondini, F. Fresi, L. Potf, and P. Castoldi, “Programmable transponder, code and differentiated filter configuration in elastic optical networks,” *J. Lightwave Tech.*, vol. 32, pp. 2079–2086, June 2014.
- [8] G. Colavolpe and T. Foggi, “Time-frequency packing for high capacity coherent optical links,” *IEEE Trans. Commun.*, vol. 62, pp. 2986–2995, Aug 2014.
- [9] J. E. Mazo, “Faster-than-Nyquist signaling,” *Bell System Tech. J.*, vol. 54, pp. 1450–1462, Oct. 1975.
- [10] F. Rusek and J. B. Anderson, “The two dimensional Mazo limit,” in *Proc. IEEE International Symposium on Information Theory*, pp. 970–974, Sep. 2005.

- [11] F. Rusek and J. B. Anderson, "Multistream faster than Nyquist signaling," *IEEE Transactions on Communications*, vol. 57, pp. 1329–1340, May 2009.
- [12] J. B. Anderson, F. Rusek, and V. Owall, "Faster-than-Nyquist signaling," *Proc. IEEE*, vol. 101, pp. 1817–1830, Aug. 2013.
- [13] D. Dasalukunte, V. Owall, F. Rusek, and J. B. Anderson, *Faster than Nyquist Signaling*. Springer, 2014.
- [14] J.-X. Cai, C. R. Davidson, A. Lucero, H. Zhang, D. G. Foursa, O. V. Sinkin, W. W. Patterson, A. N. Pilipetskii, G. Mohs, and N. S. Bergano, "20 Tbit/s transmission over 6860 km with sub-Nyquist channel spacing," *J. Lightwave Technol.*, vol. 30, pp. 651–657, Feb. 15 2012.
- [15] M. Secondini, E. Forestieri, and G. Prati, "Achievable information rate in nonlinear WDM fiber-optic systems with arbitrary modulation formats and dispersion maps," *Journal of Lightwave Technology*, vol. 31, no. 23, pp. 3839–3852, 2013.
- [16] R. G. Gallager, *Information Theory and Reliable Communication*. New York: Wiley, 1968.
- [17] N. Merhav, G. Kaplan, A. Lapidoth, and S. S. Shitz, "On information rates for mismatched decoders," *IEEE Trans. Inform. Theory*, vol. 40, pp. 1953–1967, Nov. 1994.
- [18] D. M. Arnold, H.-A. Loeliger, P. O. Vontobel, A. Kavvcic, and W. Zeng, "Simulation-based computation of information rates for channels with memory," *IEEE Trans. Inform. Theory*, vol. 52, pp. 3498–3508, Aug. 2006.
- [19] G. Ungerboeck, "Adaptive maximum-likelihood receiver for carrier-modulated data-transmission systems," *IEEE Trans. Commun.*, vol. 22, pp. 624–636, May 1974.
- [20] G. Colavolpe and A. Barbieri, "On MAP symbol detection for ISI channels using the Ungerboeck observation model," *IEEE Commun. Letters*, pp. 720–722, August 2005.
- [21] R. Bahl, J. Cocke, F. Jelinek, and R. Raviv, "Optimal decoding of linear codes for minimizing symbol error rate," *IEEE Trans. Inform. Theory*, vol. 20, pp. 284–284, Mar. 1974.
- [22] A. Modenini, F. Rusek, and G. Colavolpe, "Optimal transmit filters for ISI channels under channel shortening detection," *IEEE Trans. Commun.*, 2013.
- [23] S. ten Brink, G. Kramer, and A. Ashikhmin, "Design of low-density parity-check codes for modulation and detection," *IEEE Trans. Commun.*, vol. 52, pp. 670–678, Apr. 2004.
- [24] H. Xiao and A. H. Banihashemi, "Improved progressive-edge-growth (PEG) construction of irregular LDPC codes," *IEEE Commun. Letters*, vol. 8, pp. 715–717, Dec. 2004.
- [25] X. Hu, E. Eleftheriou, and D. M. Arnold, "Regular and irregular progressive edge-growth tanner graphs," *IEEE Trans. Inform. Theory*, vol. 51, pp. 386–398, Jan. 2005.
- [26] "Digital video broadcasting (DVB); second generation framing structure, channel coding and modulation systems for broadcasting, interactive services, news gathering and other broad-band satellite applications (DVB-S2)," Standard EN 302 307.
- [27] G. Colavolpe, T. Foggi, E. Forestieri, and G. Prati, "Robust multilevel coherent optical systems with linear processing at the receiver," *J. Lightwave Technol.*, vol. 27, pp. 2357–2369, July 2009.
- [28] F. Fresi, M. Secondini, G. Berrettini, G. Meloni, and L. Poti, "Impact of optical and electrical narrowband spectral shaping in faster than Nyquist Tb superchannel," *IEEE Photon. Technol. Lett.*, vol. 25, no. 23, pp. 2301–2303, 2013.
- [29] A. Abrardo and G. Cincotti, "Design of AWG devices for all-optical time-frequency packing," *J. Lightwave Tech.*, vol. 32, pp. 1951–1959, May 2014.
- [30] U. Mengali and M. Morelli, "Data-aided frequency estimation for burst digital transmission," *IEEE Trans. Commun.*, vol. 45, pp. 23–25, January 1997.
- [31] G. Ungerboeck, "Fractional tap-spacing equalizer and consequences for clock recovery in data modems," *IEEE Trans. Commun.*, vol. 24, pp. 856–864, Aug. 1976.
- [32] G. Colavolpe, A. Barbieri, and G. Caire, "Algorithms for iterative decoding in the presence of strong phase noise," *IEEE J. Select. Areas Commun.*, vol. 23, pp. 1748–1757, Sept 2005.
- [33] J. Hagenauer, "The turbo principle: Tutorial introduction and state of the art," in *Proc. International Symposium on Turbo Codes and Related Topics*, pp. 1–11, 1997.
- [34] L. Poti, G. Meloni, G. Berrettini, F. Fresi, T. Foggi, M. Secondini, L. Giorgi, F. Cavaliere, S. Hackett, A. Petronio, P. Nibbs, R. Forgan, A. Leong, R. Masciulli, and C. Pfander, "Sub-Nyquist field trial using time frequency packed DP-QPSK super-channel within fixed ITU-T grid," *arXiv preprint*, no. arXiv:1502.03285.
- [35] F. Rusek and A. Prlja, "Optimal channel shortening for MIMO and ISI channels," *IEEE Trans. on Wireless Commun.*, vol. 11, pp. 810–818, February 2012.
- [36] M. Secondini, D. Marsella, and E. Forestieri, "Enhanced split-step fourier method for digital backpropagation," in *Proc. European Conf. on Optical Commun. (ECOC)*, Sept. 21–25, 2014.
- [37] M. Secondini and E. Forestieri, "On XPM mitigation in WDM fiber-optic systems," *IEEE Photon. Technol. Lett.*, vol. 26, no. 22, pp. 2252–2255, 2014.
- [38] A. Carena, G. Bosco, V. Curri, P. Poggiolini, M. T. Taiba, and F. Forghieri, "Statistical characterization of PM-QPSK signals after propagation in uncompensated fiber links," in *Proc. European Conference on Optical Communication (ECOC)*, 2010. Paper P4.07.